water

MDPI

Article

Numerical Analysis of Wave Interaction with a New Ecological Quadrangular Hollow Block

Yu Wang [1,2], Dongfeng Li [2,3,*], Junwei Ye [4], Haitao Zhao [2,3], Miaohua Mao [5,6], Fuqing Bai [2,3], Jianyong Hu [2,3] and Hongwu Zhang [7]

1 School of Naval Architecture and Maritime, Zhejiang Ocean University, Zhoushan 316022, China; yuwangtt@gmail.com
2 School of Water Resources and Environmental Engineering, Zhejiang University of Water Resources and Electric Power, Hangzhou 310018, China; haitaozhao06@163.com (H.Z.); baifq@zjweu.edu.cn (F.B.); hujy@zjweu.edu.cn (J.H.)
3 Key Laboratory for Technology in Rural Water Management of Zhejiang Province, Hangzhou 310018, China
4 School of Marine Engineering Equipment, Zhejiang Ocean University, Zhoushan 316022, China; junweiyegg@gmail.com
5 CAS Key Laboratory of Coastal Environmental Processes and Ecological Remediation, Yantai Institute of Coastal Zone Research, Chinese Academy of Sciences, Yantai 264003, China; mhmao@yic.ac.cn
6 Shandong Key Laboratory of Coastal Environmental Processes, Yantai 264003, China
7 State Key Laboratory of Hydroscience and Engineering, Beijing 100084, China; zhhw@tsinghua.edu.cn
* Correspondence: lidf@zjweu.edu.cn; Tel.: +86-13588028143

Abstract: Armor blocks are extensively deployed to shield vital coastal facilities against wave erosion. Evaluating the wave run-up and reflection under wave impact is essential for the engineering design of new ecological quadrangular hollow blocks. This study constructs a three-dimensional numerical model employing the open-source CFD software OpenFOAM-v2206 to analyze these processes for the new blocks. The model's accuracy was confirmed by comparing its predictions with physical modelling tests. Model results accurately captured the variation in hydrodynamic parameters, as well as the energy dissipation properties of the new blocks. Sensitivity analysis indicated that both the wave reflection coefficients and run-up are considerably affected by mesh sizes, while velocity distributions and pressure fields were less affected by mesh. Finally, the model was utilized to examine how wave run-up and reflection for the new ecological quadrilateral hollow block are influenced by factors such as wave period, water depth, wave height, wave breaking characteristics, and wave steepness. The findings in this study provide valuable insights into novel design and safety assessment of new ecological quadrangular hollow blocks.

Keywords: numerical study; wave run-up; wave reflection; new ecological quadrilateral hollow block

Academic Editor: Georg Umgiesser

Received: 25 November 2024
Revised: 17 December 2024
Accepted: 30 December 2024
Published: 1 January 2025

Citation: Wang, Y.; Li, D.; Ye, J.; Zhao, H.; Mao, M.; Bai, F.; Hu, J.; Zhang, H. Numerical Analysis of Wave Interaction with a New Ecological Quadrangular Hollow Block. *Water* **2025**, *17*, 96. https://doi.org/10.3390/w17010096

1. Introduction

Artificial armor blocks, which could dissipate wave energy, are widely used in the protection of coastal breakwaters, sea ponds and shore protection projects. They have been studied for a long time, and various forms have been developed. In 1950, the French Sogli Consulting Company invented the first shaped artificial concrete armor blocks of Tetrapod, which was applied in the port of Casablanca, Morocco [1]. Then, Akmon, Antifer, COB, Seabee, and Accropode have been developed. Previous studies indicated that the existence of armor backs could dissipate wave energy and reduce wave run-up and reflection coefficient [2–4]. To adapt to various environmental conditions, minimize the cost, and

improve the service life of breakwater, existing blocks were optimized, and new blocks were developed. For the engineering applications, the study of the hydrodynamic performance of the armor block is of great significance, particularly its wave dissipation performance.

Although seawalls and shore protection work with artificial blocks play an important role in disaster and erosion prevention, their designs have limitations due to singular facades, rigid layouts, and poor landscape effects. The design of these blocks not only affects the aesthetics of the projects but also has negative effects on the surrounding ecological environment. Therefore, the modeling work of this study focuses on the environmentally friendly block with an innovative ecological quadrilateral hollow design.

Owing to the multitude of factors at play in real scenarios, directly analyzing and observing the dynamic interplay between waves and coastal structures is inherently challenging. As a result, wave interaction on coastal structures is typically evaluated using physical model tests. Safari et al. [5] conducted a series of two-dimensional (2D) model experiments to scrutinize the forces acting on the innovative artificial blockage structure, known as Starbloc, within a breakwater environment under typical wave conditions. Yuksel et al. [6] conducted experimental research to assess the performance of high-density cubes within breakwater armor layers, comparing outcomes against Van der Meer's formula for validation. Pardo et al. [7] studied the porosity of randomly placed concrete armor units and used high-precision laser scanning to measure the armor units. Young Hyun et al. [8] developed a new block called "Chi Block" according to the needs of the South Korean government. Through experimental verification, the conclusion is drawn that this block possesses the benefits of stability, structural integrity, economic viability, casting effectiveness, and ease of construction. Wehlitz and Schoonees [9] experimental analyses to determine the stability of Cubilok™ blocks on slopes within breakwaters, revealing that wave steepness significantly impacts the performance of these blocks.

Although physical modeling tests are the method of choice for most scholars studying armor blocks to the limitations of realistic test equipment, which are complex and costly to operate. As Computational Fluid Dynamics (CFD) advances, numerical simulation techniques can overcome the constraints of physical model testing and expand the possibilities for further research. At present, frequently utilized numerical techniques encompass the Boundary Element Method [10,11], Finite Volume Method [12,13], ALE Method [14,15], and Finite Element Method [16,17]. Additionally, there are particle-based methods like MPS [18] and SPH [19] that are also frequently utilized. In recent decades, numerous studies have explored and utilized open-source software such as OpenFOAM, SWASH [20], and SPHysics [21].

These numerical techniques have increasingly been implemented in coastal engineering applications [22–25]. Dentale et al. [26] studied the hydrodynamics characteristics of various armor blocks used in coastal defense structures. They successfully revealed the interaction between wave motion and rubble breakwaters with different armor blocks. Peng et al. [27] employed the DualSPHysics simulator to model the interaction of regular waves with artificial block slope breakwaters, effectively capturing the wave evolution on these structures. Dong et al. [28] applied the Discontinuous Deformation Analysis (DDA), a variant of the implicit DEM, to meticulously examine the dynamics and stability of caissons and armor units, factoring in the geometrical properties of the armor blocks and their interactive effects. Scaravaglione et al. [29] assessed the structural integrity of non-reinforced concrete armored units (CAU) used in gravel mound breakwaters and coastal structures by employing the finite-discrete element method (FDEM) numerical approach. Mitsui et al. [30] explored the armor block stability under solitary wave impacts, employing the SPH technique for the analysis. Under the same numerical framework, they further proved the ability of the DualSPHysics code in simulating challenging environments.

Although the experimental and numerical investigations help enhance the understanding of the hydrodynamic performance of basic and common armor blocks, these methods are not fully applicable to the new ecological quadrilateral hollow block, which requires the establishment of a more reliable numerical model. To explore the hydrodynamic responses of the new block under regular wave conditions, a computational model was developed to simulate the interaction between regular waves and a block-armored breakwater. This model was subsequently validated using the olaFlow solver on the OpenFOAM platform.

The layout of this document is outlined below: Section 2 presents a description of the new ecological quadrilateral hollow block, along with the physical model testing and numerical modeling approaches utilized in this study. Section 3 validates the model for incident regular waves, wave run-up, and reflection, and conducts the mesh resolution independence analysis. Section 4 investigates the wave profile and the flow and dynamic pressure fields around the block using various mesh sizes; it subsequently delves into the analysis and discussion of the variables that affect wave run-up and reflection characteristics of the new ecological quadrilateral hollow blocks. The results of the research are encapsulated, and suggestions are provided in Section 5.

2. Methods

2.1. Description of the Block

The geometric scale of the new ecological quadrangular hollow block [31] is 1:25. The new block is modified on the basis of the traditional quadrilateral hollow block. Drawing from the design of standard quadrilateral hollow blocks, this innovative block features a downward excavation to create a planting groove, with nine compartments strategically placed to dissipate wave energy (Figure 1). During the interaction of waves with the concrete surface of the new ecological quadrangular hollow block, the energy from waves is effectively dispersed. The design of the new ecological quadrangular hollow block could achieve stronger wave dissipation with a more stable structure. By planting coastal plants in the planting groove, the ecological functionality of the armor block is enhanced by augmenting the organic matter on the breakwater's exterior. Considering the extended period required for coastal flora to reach maturity [32–36], it is imperative to analyze the hydrodynamic properties of these protective blocks in the initial absence of coastal vegetation.

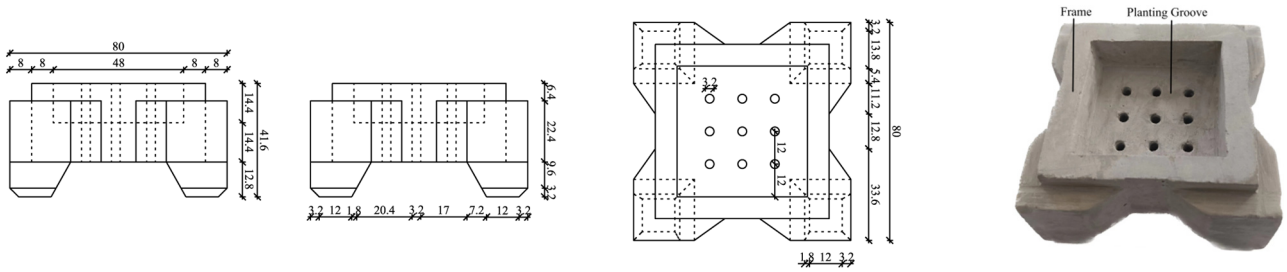

(**a**) Front view (**b**) Side view (**c**) Top view (**d**) 3D sketches

Figure 1. 2D and 3D sketches of new ecological quadrilateral hollow blocks. (unit: mm).

2.2. Physical Model Experiment

Laboratory experiments were carried out in a 2D wave tank. The dimensions of the tank are 32.0 m in length (L), 0.8 m in width (W), and 1.0 m in height (H). Waves are produced using a piston wave maker, and an active wave absorption system (AWAS) is used to dissipate the wave, which is capable of absorbing secondary reflected waves efficiently, with over 90% absorption of conventional waves (Figure 2). Wave elevations were recorded

using a DS30 multi-channel wave height acquisition system. A high-resolution video camera documented the progression and transformation of waves along the incline. In each test scenario, regular waves were employed, and each condition was tested twice to verify the consistency of the experimental results.

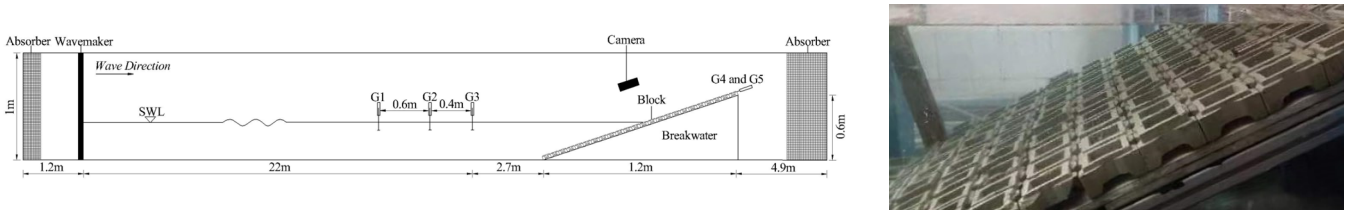

(**a**) (**b**)

Figure 2. (**a**) Diagram of model section; (**b**) Photographs of model sections.

Figure 2 is the physical flume model layout. The scaled-down test section featured a ramped construction made up of two tiers of waterproof tiles coupled with aluminum framing. The blocks were arranged in a uniform pattern along the incline. Spanning a length of 24.7 m from the wave generator to the base of the ramp, the experimental setup included wave sensors positioned at 2.7 m, 3.1 m, and 3.7 m from the slope's toe for data acquisition purposes. Data on wave surface levels was gathered with the aid of three wave sensors, which were subsequently subjected to the two-point analysis method [31] on two occasions to determine the mean wave reflection. The physical experiment reflection coefficient, denoted as K, is calculated by taking the ratio of the reflected wave's height to that of the incident wave, following the differentiation of the incident and reflected waves. To collect the data of wave run-up, a separate wave gauge is positioned adjacent to the second column of blocks on each side of the incline. Table 1 displays the experimental wave conditions corresponding to the designed numerical tests.

Table 1. Setting of wave parameters in the experiment, where d is water depth, m is slope, H represents wave height, whereas T denotes the wave period.

d (m)	m		T (s)			
			1.12	**1.79**	**2.46**	**3.13**
0.3	1.5	H (m)	0.05	0.05	0.05	0.05
	2					
	2.5					
	3		0.06	0.06	0.06	0.06
0.35	1.5					
	2					
	2.5					
	3		0.07	0.07	0.07	0.07
0.4	1.5					
	2					
	2.5		0.08	0.08	0.08	0.08
	3					

2.3. Numerical Model

For this research, a three-dimensional computational model was deployed, utilizing the Volume of Fluid (VOF) approach within the OpenFOAM CFD environment [37]. The computational model resolved the fluid dynamics by addressing the Navier-Stokes system, capturing the dynamics of the dual-phase (air and water) flow.

The three-dimensional vertical (3DV) numerical wave tank replicates the actual wave tank environment, encompassing an overall length of 30.9 m and a height of 1 m. To facilitate incident wave analysis, locations of three wave gauges were set up to be consistent with the physical model.

2.3.1. Governing Equations

The simulation of the incompressible viscous flow was governed by the Reynolds-averaged Navier-Stokes (RANS) equations, which are fundamental in capturing the dynamics of the dual-phase (air and water) flow:

$$\frac{\partial \overline{u_i}}{\partial x_i} = 0 \tag{1}$$

$$\frac{\partial \rho u_i}{\partial t} + \frac{\partial \rho u_i u_j}{\partial x_j} = -\frac{\partial p}{\partial x_i} + g_j x_j \frac{\partial \rho}{\partial x_i} + \frac{\partial}{\partial x_j} \mu \left(\frac{\partial u_i}{\partial x_j} + \frac{\partial u_j}{\partial x_i} \right) \tag{2}$$

where u is the fluid velocity, p is the dynamic pressure, ρ is the density of the water, g_j is the jth component of the gravitational acceleration, and μ is the dynamic viscosity.

The numerical simulation was conducted employing the PIMPLE algorithm within OpenFOAM, which integrates the PISO and SIMPLE methodologies. This approach effectively couples the pressure and velocity fields. Detailed descriptions of the SIMPLE and PISO algorithms are referred to in Ferziger and Perić [38] and Issa [39]. To enhance computational efficiency, adaptable time steps were employed, and the Courant number was limited to 0.3.

2.3.2. Turbulence Model

The RANS turbulence models encompass the k-ε and its RNG counterpart. The RNG model demonstrates superior accuracy, particularly in scenarios where the impact of turbulent vortices is significant. As Lara Lu et al. [40], the RNG k-ε model is more adept at managing flows characterized by high strain rates and pronounced streamline curvature. Consequently, RNG k-ε was chosen for the computational analysis.

When Reynolds numbers are high, the equations of k and ε are as follows:

$$\frac{\partial k}{\partial t} + \overline{u_j} \frac{\partial k}{\partial x_i} = \frac{\partial}{\partial x_i} \left(\frac{\mu_T}{\sigma_k} \frac{\partial k}{\partial x_j} \right) + G_k - \varepsilon \tag{3}$$

$$\frac{\partial \varepsilon}{\partial t} + \vec{u_j} \frac{\partial \varepsilon}{\partial x_i} = \frac{\partial}{\partial x_i} \left(\frac{\mu_T}{\sigma_\sigma} \frac{\partial \varepsilon}{\partial x_j} \right) + C^*_{1\varepsilon} \frac{\varepsilon}{k} G_k - C_{2\varepsilon} \rho \frac{\varepsilon^2}{k} \tag{4}$$

where $G_k = 2\mu_T \overline{D_{ij} D_{ij}}$ is the turbulent kinetic energy generation term, and $D_{ij} = (\partial \overline{\mu_i}/\partial x_j + \partial \overline{\mu_j}/\partial x_i)/2$ is the mean strain rate tensor. $C^*{}_{1\varepsilon} = C_{1\varepsilon} - \eta(1 - \eta/\eta_0)(1 + \beta\eta^3)$, where $\eta = Sk/\varepsilon, S = \left(2\overline{D_{ij} D_{ij}}\right)^{1/2}$. Where C_μ = 0.0845, σ_K = 1.39, σ_ε = 1.39, $C_{1\varepsilon}$ = 1.42, $C_{2\varepsilon}$ = 1.68, η_0 = 4.38, β = 0.012.

2.3.3. Boundary Condition

Figure 3 depicts the boundary specifications for the computational model. A relaxation zone is established at the inlet to facilitate wave generation and absorption. The top

boundary, representing the atmosphere, functions as an open boundary, allowing both liquid and gas to exit the simulation area, with air being the only medium that can re-enter. The slope, armor block, outlet, and bottom are configured with a non-slip stationary wall boundary condition. The side boundaries are designated as Symmetry Plane.

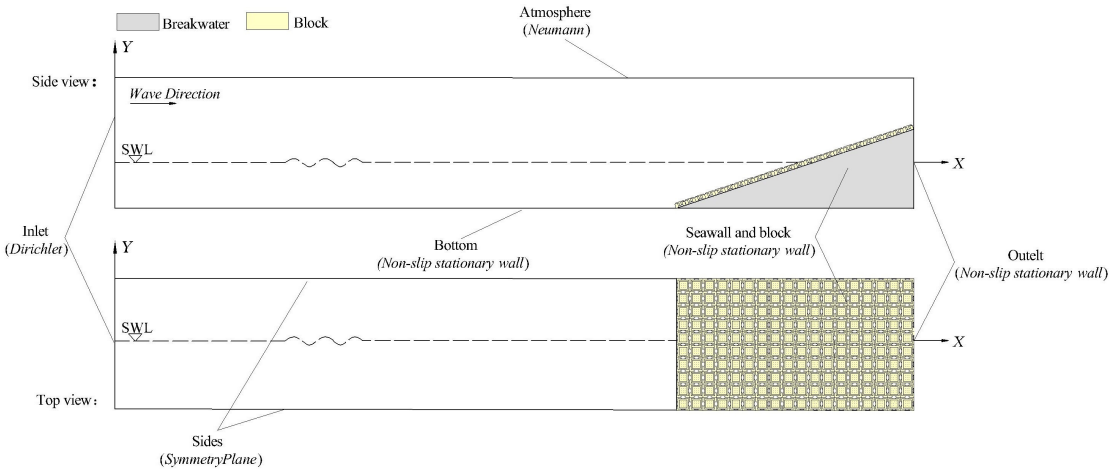

Figure 3. Boundary conditions for the numerical model.

2.3.4. Mesh Generation

For the accurate replication of wave propagation and the ensuing structural interactions, the developed numerical model utilizes a non-uniform mesh system during the meshing phase. Figure 4a illustrates that the mesh density is higher near the water-air interface and the area surrounding the structure. The mesh tools SnappyHexMesh and blockMesh in the OpenFOAM library are used to generate the mesh. Jacobsen and Fuhrman [41] have suggested employing square grid cells for enhanced simulation accuracy in the context of nonlinear wave modeling. In this study, blockMesh is used to create a square basic mesh, and SnappyHexMesh is used to remove the quadrangular hollow blocks.

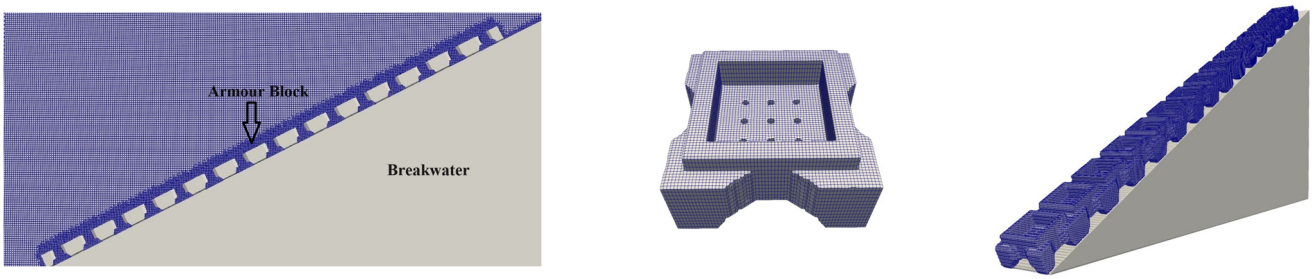

Figure 4. (**a**) Meshes around breakwater and blocks; (**b**) Meshes on a single block; (**c**) Meshes on a column of blocks.

Vanneste and Troch [42] have indicated that the arrangement of mesh points corresponds to the characteristics of the waves, with the mesh dimension in the x/y-axis ($\Delta x/y$) being associated with the wavelength-to-height ratio (L/H). The mesh size near the water surface is set at $\Delta x = L_{min}/100, \Delta y = H_{min}/10$. $L_{\min}$ and $H_{\min}$ are the minimum values of L and H. According to the setup of wave conditions, Δx = 0.0025 m, $\Delta y = \Delta z$ = 0.005 m. Table 2 details the distribution of mesh resolutions across the model's domain.

Table 2. Mesh size for different regions.

Mesh Region	Mesh Size $\Delta x \times \Delta y \times \Delta z$ (m)
Most region	$0.01 \times 0.01 \times 0.01$
In close proximity to the water surface	$0.005 \times 0.005 \times 0.005$
In the vicinity of the breakwater and blocks	$0.0025 \times 0.0025 \times 0.0025$

When generating meshes in proximity to the armor block based on the physical model, their number is overly large (~tens of millions). To enhance computational efficiency, Ye et al. [43] only set one row of Accropode on the armor breakwater, which does not affect the numerical results. To simplify and improve the computation, blocks in the model are arranged only in one column.

2.3.5. Skill Metrics

To determine the level of agreement between the computational outcomes and empirical data, the Pearson correlation coefficient r is used:

$$\mathrm{r} = \frac{\sum_{i=1}^{n}(\eta_{measured} - \overline{\eta_{measured}})(\eta_{numerical} - \overline{\eta_{numerical}})}{\sqrt{\sum_{i=1}^{n}(\eta_{measured} - \overline{\eta_{measured}})^2}\sqrt{\sum_{i=1}^{n}(\eta_{numerical} - \overline{\eta_{numerical}})^2}} \quad (5)$$

where n is the sample size, η is the value of the variable, and $\overline{\eta}$ is the sample mean.

To obtain the discrepancy between the numerical and experimental values, the Root Mean Square Error (RMSE) is utilized, it is calculated by the formula:

$$\mathrm{RMSE} = \sqrt{\frac{1}{n}\sum_{i=1}^{n}(\varphi_{numerical} - \varphi_{measured})^2} \quad (6)$$

where $\varphi_{numerical}$ and $\varphi_{measured_i}$ are the numerical and measured results, respectively.

3. Model Validations

3.1. Validation of Incident Regular Waves

To evaluate the accuracy of OpenFOAM in replicating regular incident waves, we compared the modeled wave surface results from 'bare' flumes (i.e., without any model present) with theoretical predictions and experimental data. This validation was conducted under three different conditions. A total of 12 sets of unstructured wave flume tests, typical of 3 groups of working conditions, were taken for validation. The wave parameter used in this study corresponds to the target wave, and the numerical wavemaker in OpenFOAM is grounded on the second-order Stokes' theory of wave, which is a well-established framework for simulating wave generation and propagation. The wave profiles captured at G1 serve to verify the accuracy of the numerical model.

Figure 5 illustrates the temporal variation of water surface elevations in 'bare' flumes, as captured by theoretical calculations, numerical simulations, and experimental measurements. Due to the initial instability of the physical wave-making system (e.g., affecting the first few waves), the physical wavemaker works stably after t = 20 s, which agrees well with the numerical results (Figure 5). Waveforms obtained from the theoretical calculations and numerical simulations are close to each other well. The Pearson correlation coefficients between the theoretical predictions and numerical outcomes were 0.9986, 0.9988, and 0.9981 for d = 0.3 m, 0.35 m, and 0.4 m. Figure 5 displays the comparison of water level changes between experimental data and numerical simulations, of which the Pearson correlation coefficients were 0.9968, 0.9981, and 0.9972, respectively. Because of the viscosity, a slight

attenuation of wave heights is observed in the numerical flume, which does not affect the overall results.

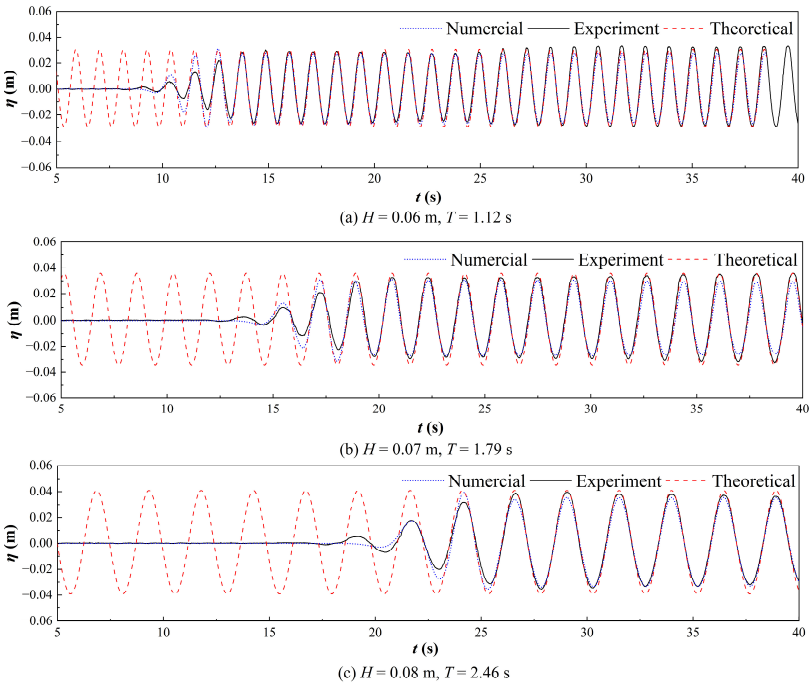

Figure 5. Temporal variations of theoretical, numerical and experiment values of water level heights in "bare" flumes.

The wave generator within olaFlow accurately reproduces a range of basic wave types. Upon commencement of wave generation by olaFlow, the wave height promptly stabilizes at the anticipated level. The absence of wave height reduction and interference effects confirms that olaFlow effectively and successfully manages incident wave absorption at the terminal boundary through the application of active wave absorption boundary conditions.

3.2. Validation of Wave Run-Up Height and Reflection Coefficient

A total of 36 scenarios were modeled, including typical wave conditions in the experiment. Figure 6 indicates that the relative run-up height (R/H) and reflection coefficients (K_r) produced from OpenFOAM agree well with the experimental results during physical modeling campaigns. In all cases, the OpenFOAM model underestimates R/H and K_r.

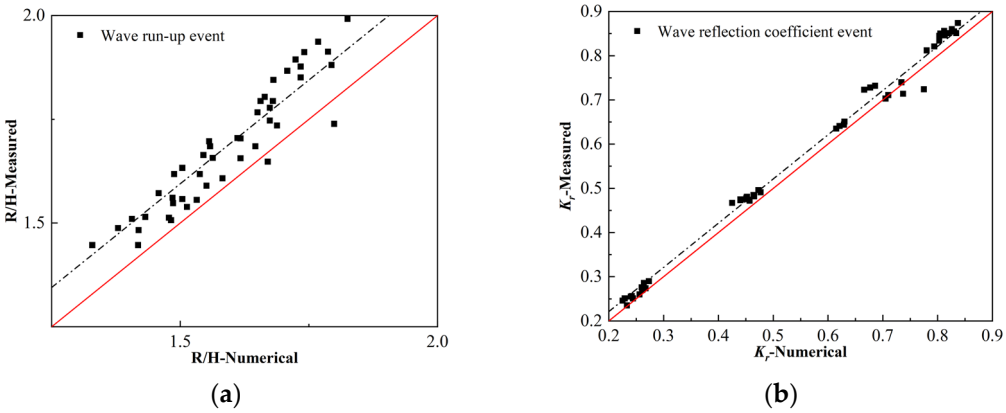

Figure 6. Scatterplots between the measured and numerical values for the (**a**) relative run-up height and (**b**) reflection coefficient events. Note: The red lines are the ones of perfect agreement, and the black dashed lines are the fitted lines.

Overall, R/H and K_r were underestimated in OpenFOAM. The bias (average ratio of predicted to the measured dimensionless flows) was 0.998 times, i.e., the numerical model overestimated the measured relative run-up height and reflection coefficient by a factor of 0.998 on average of the 36 cases, where wave run-up occurred. The RMSE values for the relative wave run-up height and reflection coefficient are 0.29 and 0.077. While the numerical R/H and K_r slightly fall short of the empirical data, this minor underprediction does not significantly affect the understanding of the run-up and reflection dynamics of the armor block.

3.3. Mesh Resolution Independence Analysis

The mesh size near the block is set $\Delta x = \Delta y = \Delta z = 0.005$ m, and the total mesh number is 96,912 (Mesh III). The mesh size in the base case is set $\Delta x = \Delta y = \Delta z = 0.0025$ m, and the total mesh number is 763,416 (Mesh II). Mesh size in case I is set $\Delta x = \Delta y = \Delta z = 0.00125$ m, and its total number is 5,549,943.

To assess how the mesh resolution impacts the computational outcomes, the extrapolated relative error (ERE) was calculated, which is expressed as follows:

$$ERE_{21} = \left| \frac{\Psi_{ext}^{21} - \Psi_1}{\Psi_{ext}^{21}} \right| \tag{7}$$

The extrapolated value is:

$$\Psi_{ext}^{21} = (r_{21}^n \Psi_1 - \Psi_2)/(r_{21}^n - 1) \tag{8}$$

$$n = \frac{1}{lnr_{21}} |\ln(\delta_{32}/\delta_{21}) + q(n)| \tag{9}$$

$$q(n) = \ln\left(\frac{r_{21}^n - p'}{r_{32}^n - p'}\right) \tag{10}$$

$$p' = Sign(\delta_{32}/\delta_{21}) \tag{11}$$

where $\delta_{32} = \Psi_3 - \Psi_1$, $\delta_{21} = \Psi_2 - \Psi_1$, $r_{21} = s_2/s_1$ and $r_{32} = s_3/s_2$. Ψ is the computational result of the mesh. Sign represents a sign function. When $p' = 1$, it indicates monotonic convergence or divergence, and when $p' = -1$, it indicates oscillatory convergence.

Table 3 presents the Error Relative to Experiment (ERE) for both wave run-up height and reflection coefficient under Wave-I (and II and III) conditions with $d = 0.3$ m (0.35 m and 0.4 m), $H = 0.05$ m, and $T = 1.79$ s, which were 7.181% (8.473% and 9.387%) and 0.898% (2.955% and 6.946%). Increasing the mesh size from 0.00125 m to 0.0025 m has a minimal impact on the ERE, indicating that Mesh II is adequate for achieving precise simulation outcomes.

Table 3. Run-up and reflection coefficient values for different meshes for three wave conditions.

	Coefficients	**Wave-I**	**Wave-II**	**Wave-III**
Mesh I	R (m)	0.0823	0.0865	0.0901
	K_r	0.512	0.508	0.517
Mesh II	R (m)	0.0782	0.0834	0.0861
	K_r	0.491	0.482	0.496
Mesh III	R (m)	0.07146	0.0791	0.0833
	K_r	0.4872	0.4723	0.4824
Ψ_{ext}^{21}	R (m)	0.08867	0.09451	0.09943
	K_r	0.51664	0.52345	0.55559

Figure 7 shows comparisons of the R/H and K_r from two groups of meshes. Due to the numerical dissipation in the computational model, it is difficult to fully accurately simulate the small wave breaking on the surface of the experimental block, the overall prediction results are underestimated. Mesh III was not analyzed due to poor accuracy. Results of the R/H and K_r from meshes I and II are both very close to the experimental ones (e.g., RMSE = 0.27 and 0.29 (0.077 and 0.091) from Mesh I and II for the R/H (K_r). Taking into account the equilibrium between numerical precision and processing velocity, Mesh II was selected for the following calculations.

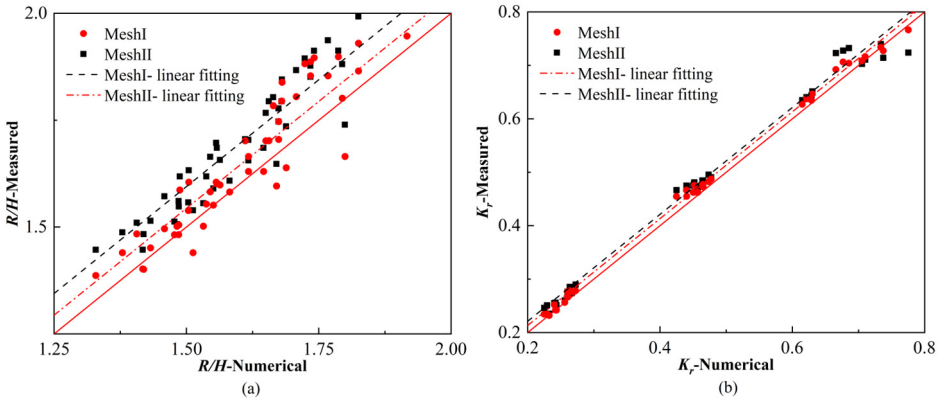

Figure 7. Comparisons of (**a**) relative run-up and (**b**) reflection coefficient values between Mesh I and II. Note: The red lines are the ones of perfect agreement.

4. Results and Discussion

Although olaFlow's numerical wavemaker has been tested without structures, it remains to be further verified whether the olaFlow-based computational model of wave-new ecological quadrilateral hollow block interaction can reliably simulate the complex interaction process. To perform the numerical simulation efficiently, 96 CPU cores were employed for parallelization. The CPU type is 2× AMD EPYC 7643 with 2.3 GHz.

4.1. Wave Profile and Wave Fields Evolution with Different Meshes

The wave height gauges G1, G2, and G3 are located at 21 m, 21.6 m, and 22 m from the wave-maker. Figure 8 depicts the temporal progression of water surface elevations for three distinct series, each employing different mesh densities. The test was conducted at T = 1.79 s and H = 0.05 m. G1and G2 showed a nonlinear state, and the wave valley became steeper compared with that of G1. The sub-wave peaks appeared in G1 and G2 close to the new ecological quadrilateral hollow blocks, where the incident waves were reflected, superimposed, and broken. The wave heights corresponding to G3, G2, and G1 decrease sequentially due to the dissipation processes after contacting the blocks.

Figure 8 illustrates the temporal variations in water surface elevations derived from the experimental configuration, which exhibits significant nonlinear characteristics by including the structure into the flume. This nonlinearity stems from the inherent inaccuracies of the experimental setup and the pronounced wave-structure interaction, which significantly contributes to the observed nonlinear effects, with the latter particularly contributing to pronounced nonlinear effects noticeable at the wave trough.

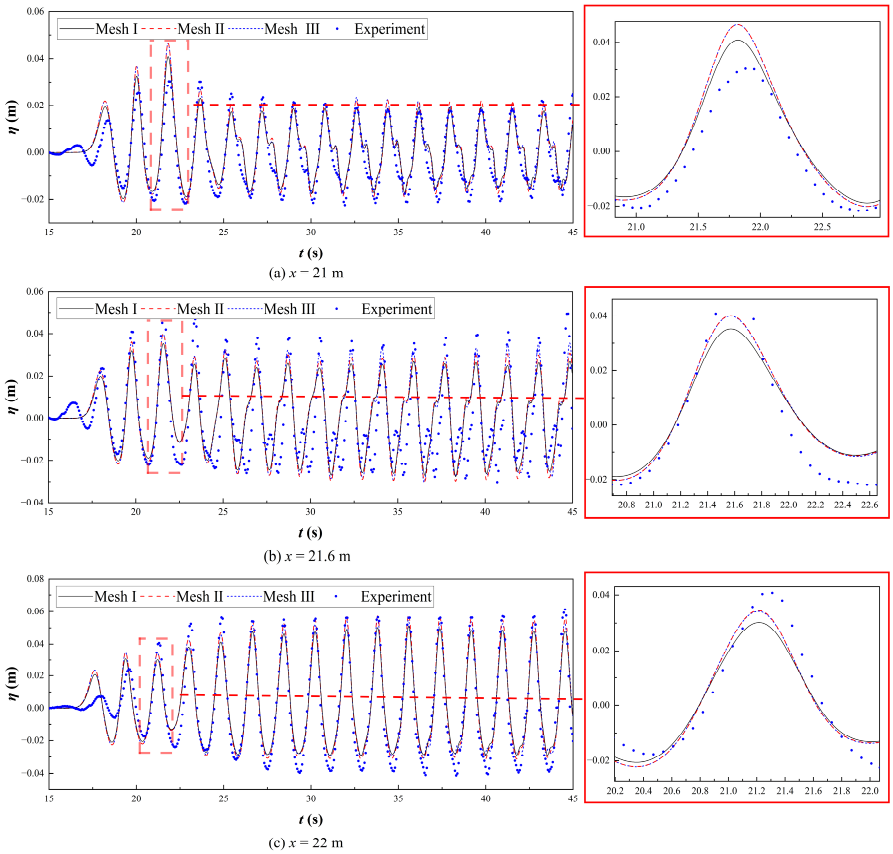

Figure 8. Temporal sequences of water surface elevations at locations G1, G2, and G3 with various mesh sizes.

Figure 9 shows the velocity fields using various meshes for the same wave condition at t = 12 s. At this point, the wave climbed to its highest point, and the velocity fields using various meshes are in general agreement with each other. The peak flow rate is predominantly found at the point where the leading edge of the wave makes contact with the obstruction. Although the wave run-up height reaches its peak, the flow velocity is reduced. The flow velocity vector is oriented upwards along the entire incline. When the wave reaches the highest block, the flow velocities on the surface and inside the block are large, and the acting direction shows irregularity. The wave climbs the highest before breaking. The velocity of the flow at the liquid's surface exhibits non-linear characteristics, in all these cases, the direction of the flow velocity action is upward. Mesh I presents a slightly larger flow velocity than Mesh II and Mesh III. The flow velocity using Mesh I at the very front of the wave is distributed in more directions, while the least velocity component upwards is shown in Mesh III. This occurrence can be rationalized by the increased fidelity of the model's finer meshes, which more accurately reflect actual conditions.

Figure 10 shows the distribution of the dynamic pressure fields from three mesh settings under the same wave condition at t = 12 s. The distribution of the positive pressure zone at the wave's leading edge is uneven, a result of the intense interaction between the wave and the block. Upon attaining its peak run-up elevation, the substantial pressure exerted by the water mass is conveyed to the wave's forefront through the wave's movement, accompanied by a significant dissipation of wave energy.

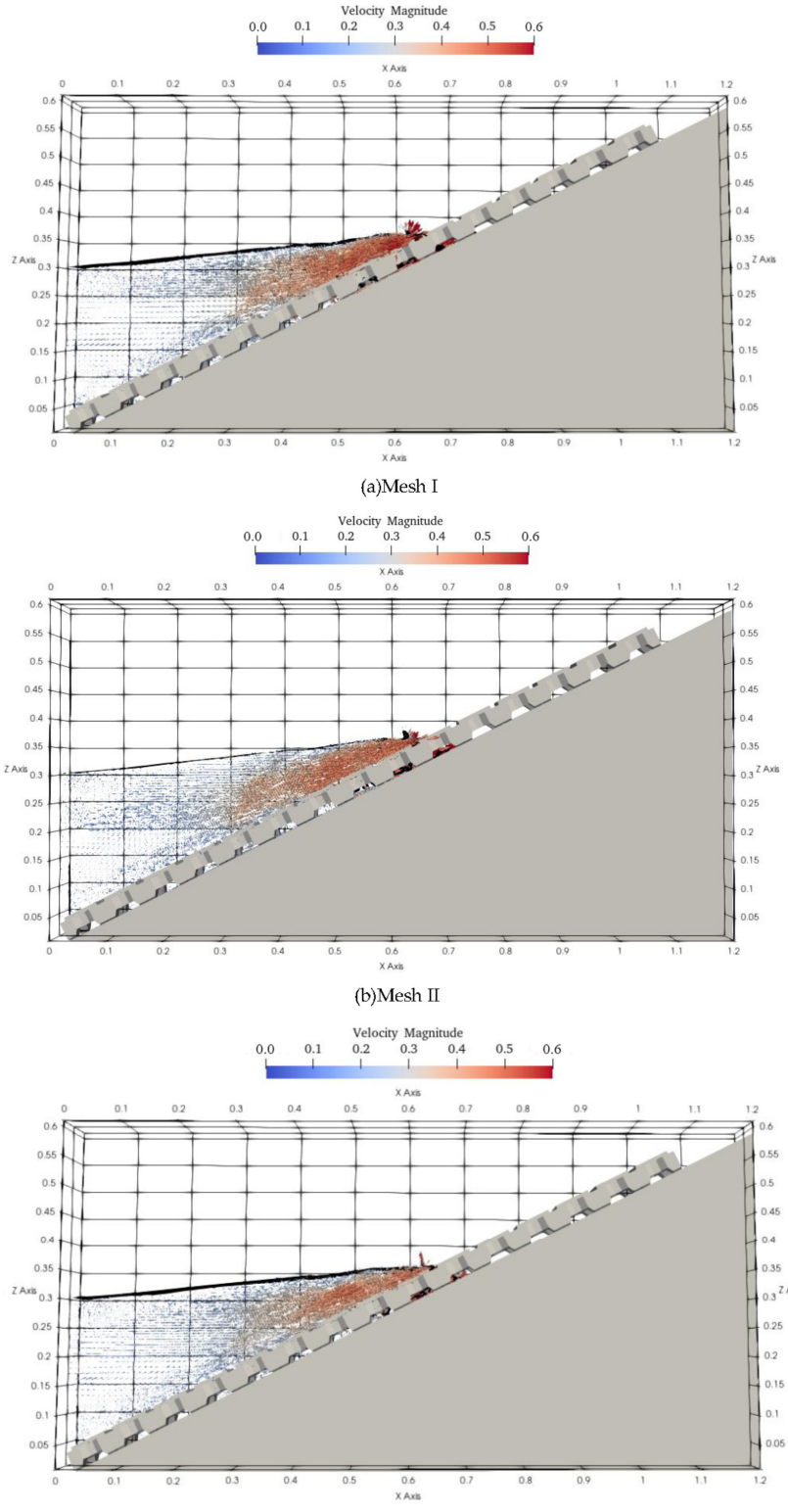

Figure 9. Comparison of flow velocity vectors among meshes (**a**) I, (**b**) II, and (**c**) III.

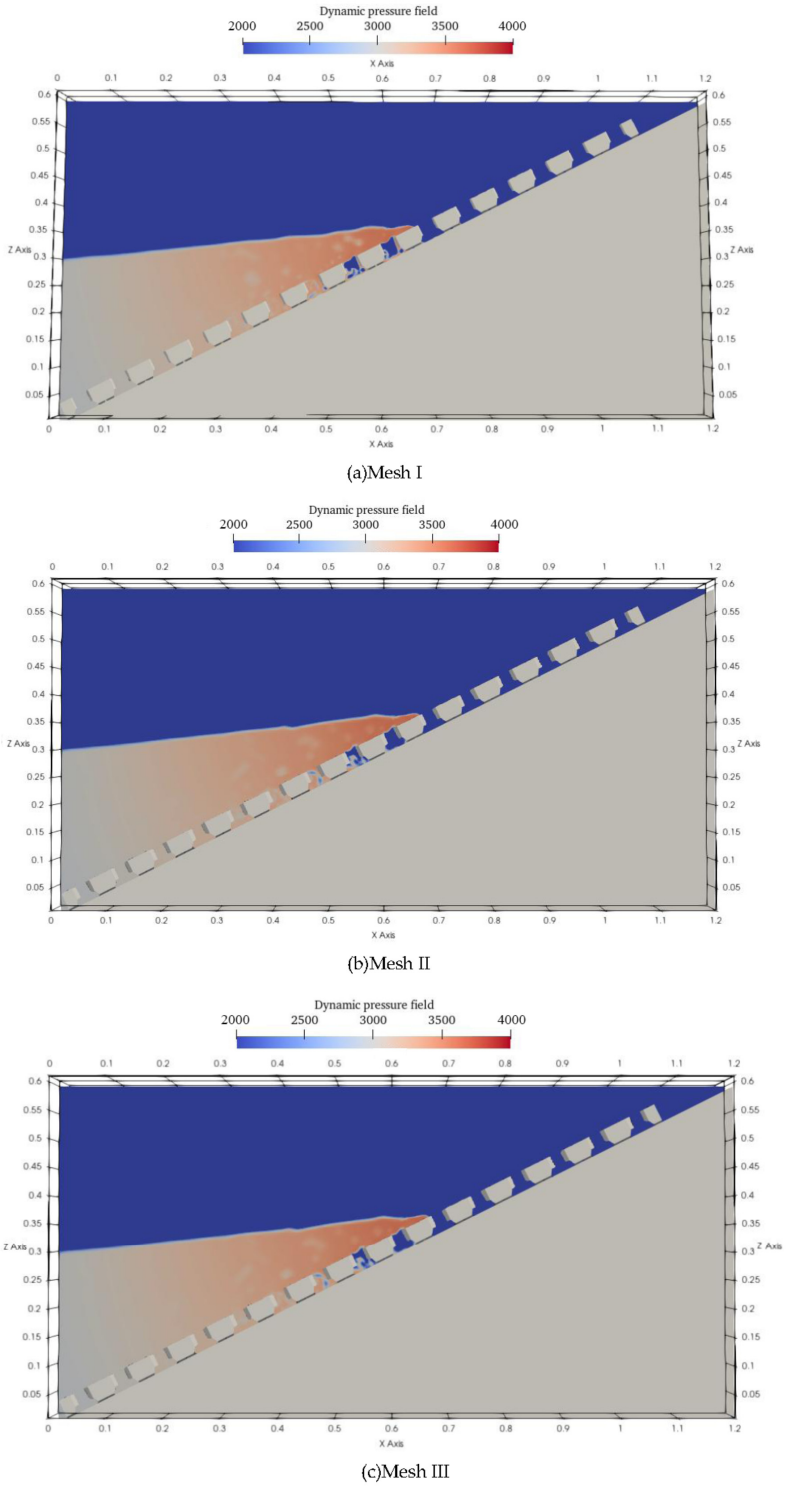

Figure 10. Comparison of dynamic pressure fields for different meshes.

4.2. Wave Velocity and Turbulent Flow

Figure 11 illustrates the wave pattern and the distribution of velocity with T = 1.79 s and H = 0.06 m. When wave climbs the incline, a region characterized by peak flow velocity is observed right at the leading edge of the wave. At high flow velocities, the wave continues running up the slope until its height reaches the maximum; the flow velocity decreases and only the water remaining inside the block has a higher flow velocity. When the wave falls back, the velocity of the flow augments at the wave's leading section upon its interaction with the block. During the whole wave impact cycle, the flow velocity is

elevated at the upper regions of the block as the wave ascends the incline. Conversely, as the wave's run-up reaches its maximum and then begins to ebb, the velocity within the block's central and lower regions increases.

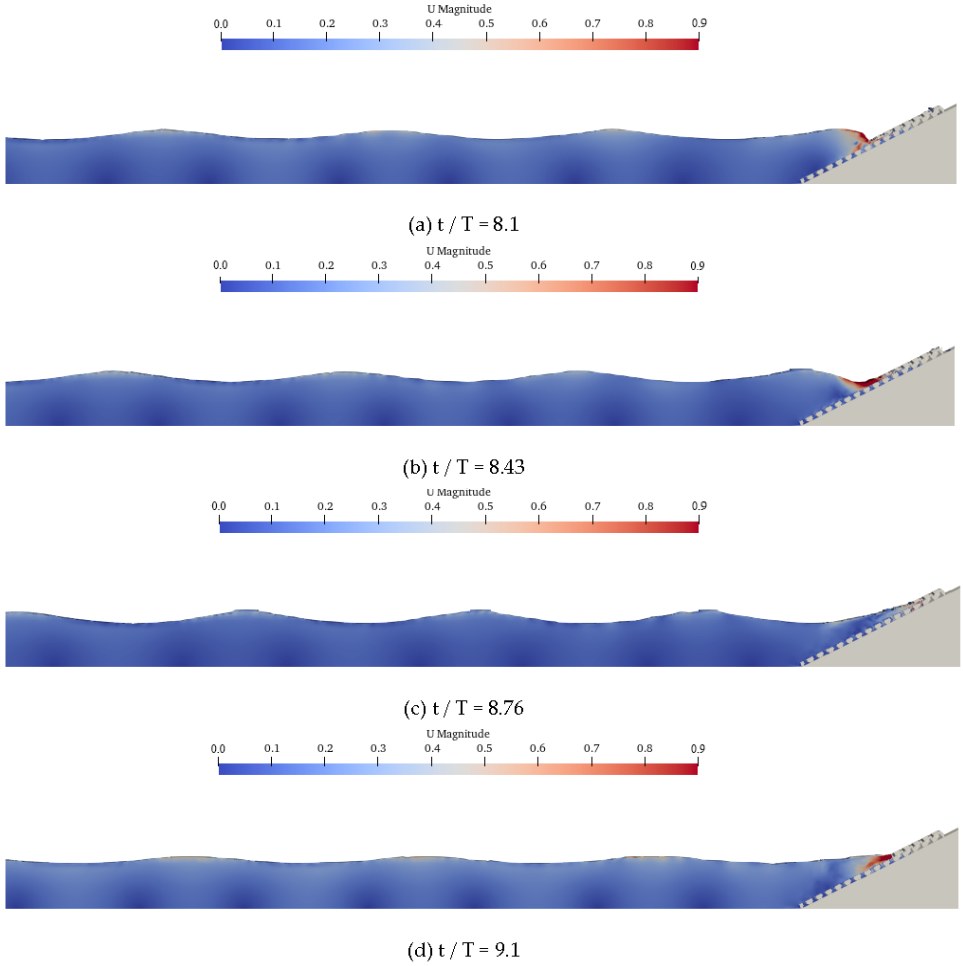

Figure 11. Wave patterns and velocity distribution when the wave propagates to the breakwater.

Figure 12 portrays the pattern of turbulent kinetic energy dissipation as waves engage with new ecological quadrangular hollow blocks at T = 1.79 s and H = 0.06 m. The water body consumes turbulent kinetic energy as wave run-up develops. The main mechanism controlling the dissipation is the contact and slap between the leading edge of the water mass and the surface of the block. The wave interacts with the embankment surface during the run-up, and the corresponding energy loss increases, which suggests a reduction in wave reflection. As the wave surges upward, the area of significant energy dissipation is predominantly located in the upper section of the block (Figure 12a–d). When the wave is running up to reach the highest level and then falling, the region of intense dissipation predominantly occupies the interior and lower sections of the block (Figure 12e–h). The interaction between the wave and new ecological armor blocks significantly produces the turbulent kinetic energy and the corresponding dissipation rate in the water body.

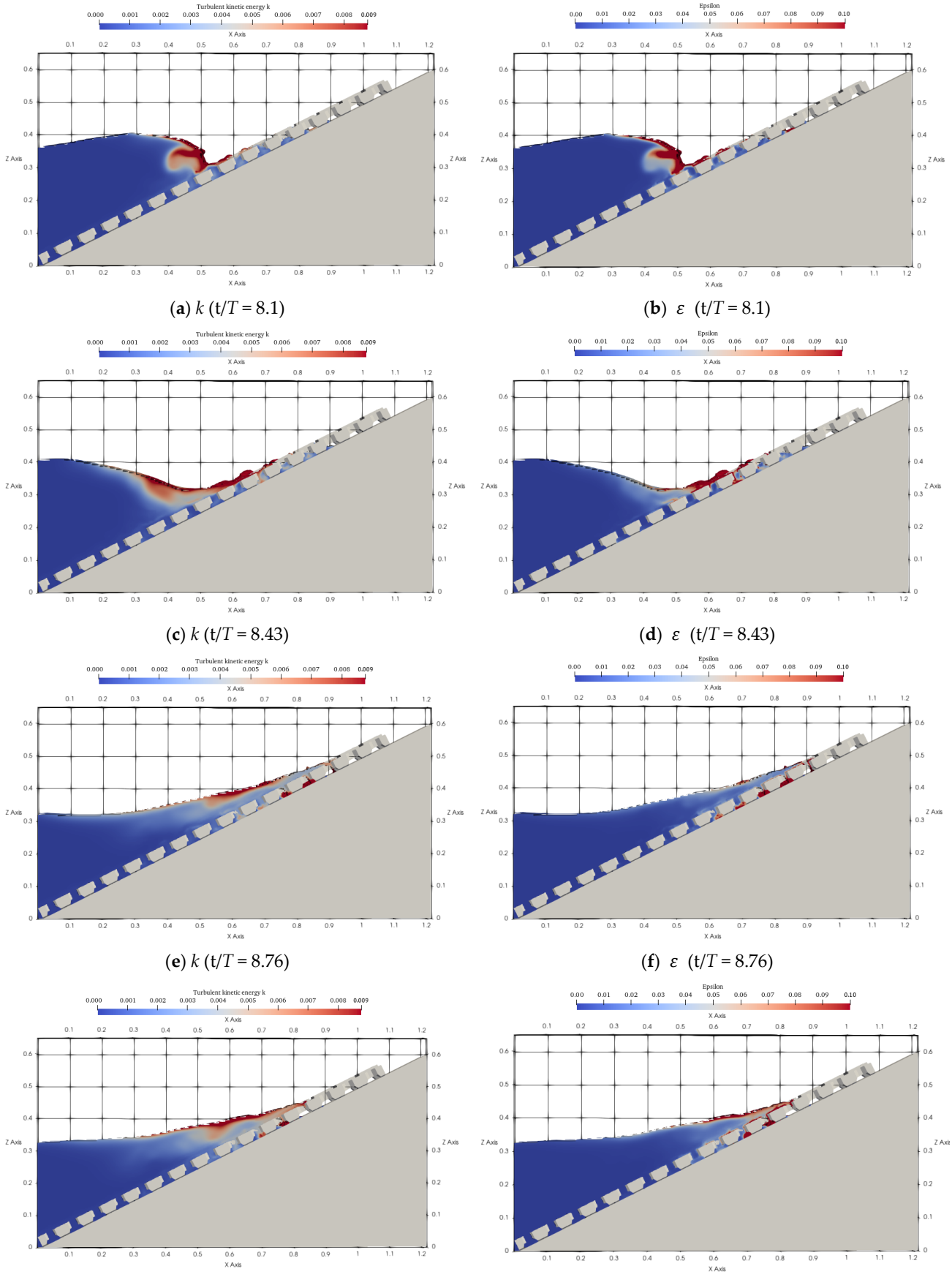

(**a**) k (t/T = 8.1) (**b**) ε (t/T = 8.1)

(**c**) k (t/T = 8.43) (**d**) ε (t/T = 8.43)

(**e**) k (t/T = 8.76) (**f**) ε (t/T = 8.76)

(**g**) k (t/T = 9.1) (**h**) ε (t/T = 9.1)

Figure 12. Distributions of (**a**,**c**,**e**,**g**) turbulent kinetic energy and (**b**,**d**,**f**,**h**) dissipation rate.

4.3. Wave Run-Up

For irregular waves, the run-up height is typically denoted as $R_{u2\%}$ [44], which signifies the level of run-up surpassed by only 2% of the incoming waves [45]. Schoonees et al. [44] determined the wave run-up for regular waves by sorting the rise heights in descending order for each test and then computing the rise height that was surpassed by only 2% of the waves. Figure 13 illustrates how the R is affected by variations in wave height and period. At a period of 1.79 s, the wave run-up height escalates in correlation with the wave height (H). It is observed for three different sets of water depths. With d = 0.35 m, there is a more pronounced rise in wave run-up height compared to the other two scenarios, which is consistent with the measured results; the run-up height escalates in correlation with the period, as depicted in Figure 13b. Changes in run-up are highly correlated with the wave period. The modeled wave run-up slightly increases when T = 1.79 s and H = 0.07 m, due to its underestimation of turbulent dissipation. The average RMSE values shown in Figure 13a,b are 0.011 m and 0.0068 m, respectively.

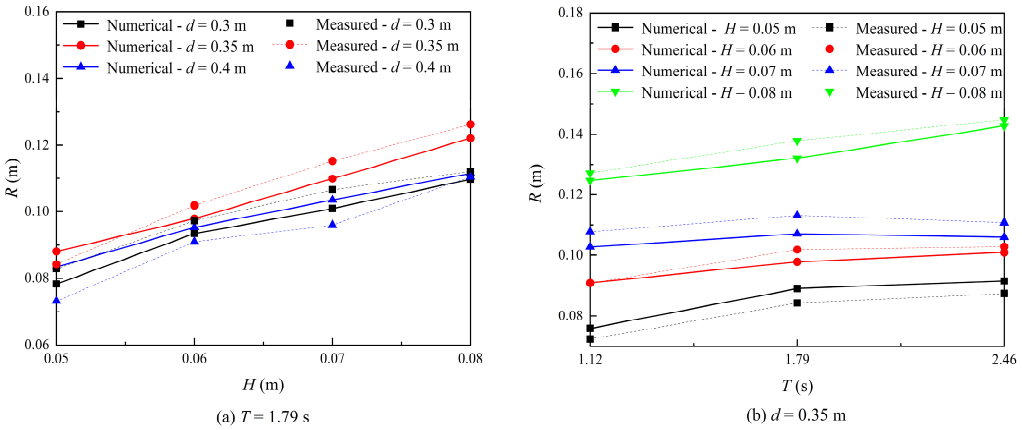

Figure 13. Variations of R with H and T.

The left-hand panel of Figure 14 displays how varying water depths affect R under conditions of differing wave heights. With the increase of relative water depth (the ratio of water depth d to wavelength L (d/L)), the wave run-up height generally exhibits an upward tendency. When H = 0.05 m, R tends to increase in response to an increase in the ratio of d/L. When H > 0.05 m, R achieves its maximum at d/L = 0.179. Under shallow water waves (d/L < 0.5), upon reaching a certain extent in d/L, wave energy is diminished by bottom friction, leading to a reduction in R. When H increases, this trend is more obvious. Elevated H precipitates earlier wave breaking, consequently diminishing R, a phenomenon particularly evident at H = 0.08 m.

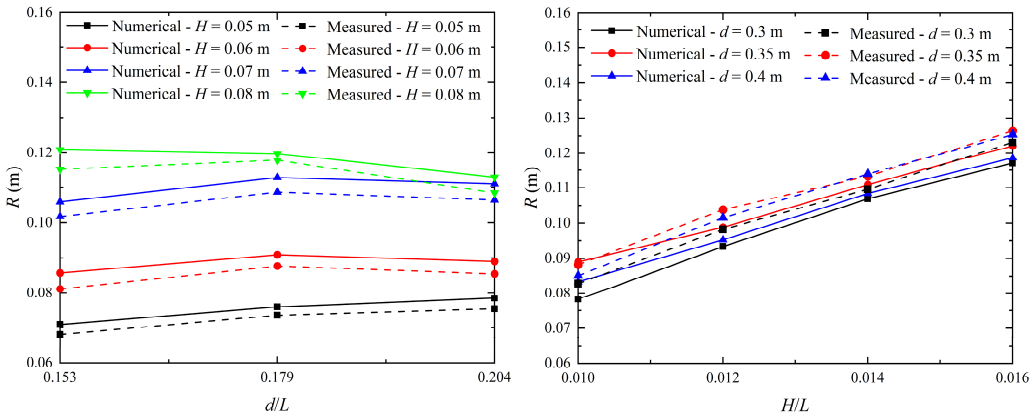

Figure 14. Variations of R with d/L and H/L.

Wave steepness, which is the proportion of the wave height (H) relative to its wavelength (L) (i.e., $S = H/L$), the R over various d/L, as illustrated in the right-hand panel of Figure 14. As wave steepness augments, so does R. The correlation between wave steepness and R exhibits a consistent upward trend across varying water depths.

The Iribarren number, also known as the surf similarity parameter [46], is given by the formula $\xi_{m-1,0} = tan\alpha/(H_{m0}/L_{m-1,0})^{1/2}$, where α is the angle between the slope and the bottom, and $\tan\alpha$ is equal to slope ratio $1/m$ in this paper, and L is the wavelength in deep water $L = gT^2/(2\pi)$. The scatter plot of relative wave run-up height and the surf similarity parameter is shown in Figure 15. As the surf similarity parameter escalates, R/H also increases. However, the correlation between the surf similarity parameter and R/H is not uniformly decreasing when there are variations in wave height and period. This situation depends on the specific measurements of H and T; the surf similarity parameter does not solely dictate the relative wave run-up height. It is not a straightforward linear association with R/H but rather influences the pattern of its variation.

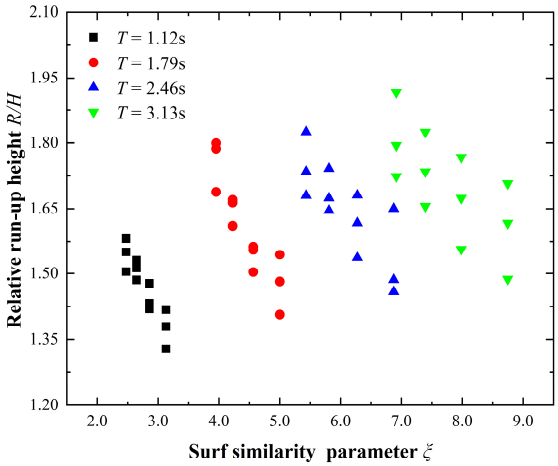

Figure 15. Scatter plot of R/H changing with ξ.

4.4. Comparison with Existing Wave Run-Up Formulas

Table 4 enumerates various existing formulas for wave run-up. In the realm of wave run-up studies, a dimensionless number is obtained by dividing the run-up by the incident wave height, which is usually expressed as a surf similarity parameter [47–51]. Figure 16 shows the relationship between R predicted by different methods and experiment value. Line 1: 1 indicates that the predicted value is completely consistent with the experimental value under ideal conditions. The run-up data points of numerical simulation are closely distributed near the line 1: 1. The value obtained by Muttray M.'s formula is close to the experimental value. The data near the line 1: 1 are generally lower than the experimental value, and in the experimental value range of 1.4–1.6, there are some data that are more than twice the experimental value. The predicted value obtained using the Hunt [52] formula is generally around line 1: 1. The run-up height prediction value obtained by Van der meer and Stam's formula is very different from the experimental value. This equation is typically employed for determining the run-up of irregular waves. The predicted values obtained by Saville [53] and Whaline et al. [54] are larger than the experimental values. Through comparison, it is found that there are some deviations in the above formulas, which are related to the applicable conditions of the formulas, and need to be further adjusted and verified under specific wave conditions.

Table 4. Wave run-up formulas.

Authors	Structure Types	Formulas	Remarks
Van Der Meer and Stam [49]	Smooth impermeable slopes	$\frac{R_{U2\%}}{H_S} = 1.5\gamma\xi_{max}$	H_S is the signifcant wave height, γ is the reduction factor
Muttray M, Oumeraci H, Oever E [50]	Rubble mound breakwaters with steep front slope	$R = 1.31H_i(1 + C_r)$, $C_r = \frac{H_r}{H_i}$	H_r is the reflected wave height, H_i is the incident wave height
Hunt [52]	Impermeable slopes	$\frac{R}{H_0} = \xi = \frac{\tan\alpha}{\sqrt{H_0/L_0}}$	$\tan\alpha$ is the slope, H_0 and L_0 are the deep-water wave height and length
Saville [53] and Whalin et al. [54]	Small beach slopes	$\frac{R}{H} = \frac{\tan\beta}{\left(\frac{H_0}{L_0}\right)^{0.4}}$	H_0 and L_0 are the deep-water wave height and length

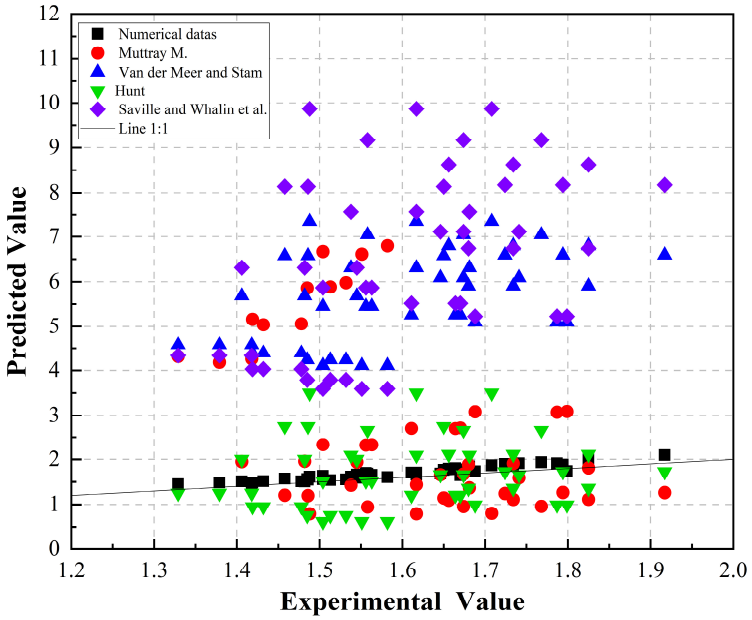

Figure 16. Comparison of numerical wave run-up results with existing wave run-up formulas. Note: The formulas of Van Der Meer and Stam [49], Muttray M, Oumeraci H, Oever E [50], Hunt [52], Saville [53] and Whalin et al. [54] are in Table 4.

4.5. Wave Reflection

The technique developed (two-point method) by Goda and Suzuki [31] is utilized to distinguish between the incident and reflected waves. Post-separation, the height of the reflected wave is divided by that of the incident wave, yielding the reflection coefficient, denoted as *Kr*.

Figure 17 illustrates how wave height and period affect the reflection coefficient. In Figure 17a, it can be observed that the wave reflection coefficients decline as wave height increases, specifically at a period of 1.79 s. The numerical model slightly underestimates K_r when H = 0.05 m, as it dissipates more energy in the armor block. In Figure 17b, at d = 0.35 m, *Kr* tends to increase with the wave period's lengthening. The numerical model agrees with the physical results well. The average RMSEs values in Figure 17a,b are 0.0055 and 0.22, respectively.

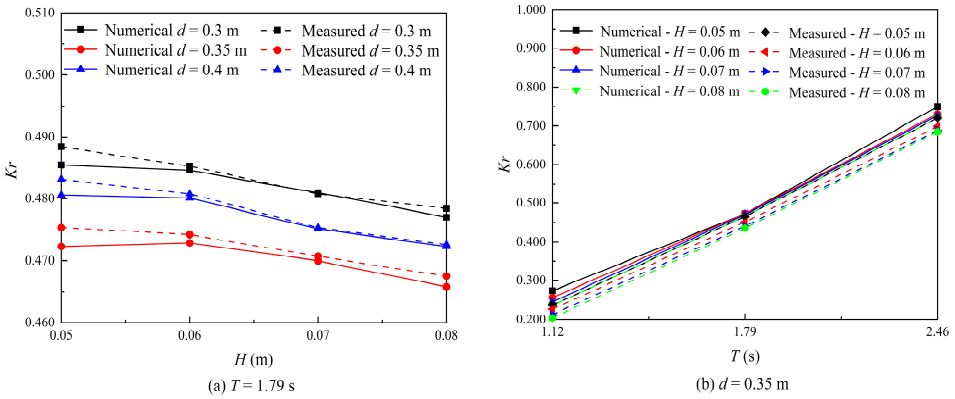

Figure 17. Variations of reflection coefficients with (**a**) H and (**b**) T.

Figure 18 demonstrates the influence of relative water depth on Kr across various wave height scenarios. With the gradual deepening of the relative water depth, the wave reflection coefficient in the vicinity of the block tends to diminish gradually; for example, at H = 0.06 m, the reflection coefficient drops from 0.268 to 0.255 as the relative water depth increases from 0.153 to 0.204. Wave velocities are elevated near the blocks during the phases of wave run-up and retreat, where greater energy dissipation occurs, leading to diminished reflection coefficients. With the ongoing deepening of d/L, the wave along the course of the run-up shows stronger energy loss and turbulent energy dissipation inside the block. Consequently, the energy of the receding water mass diminishes, correspondingly reducing the energy of the reflected wave, which is finally manifested in the reduction of the reflection coefficient in front of the armor block.

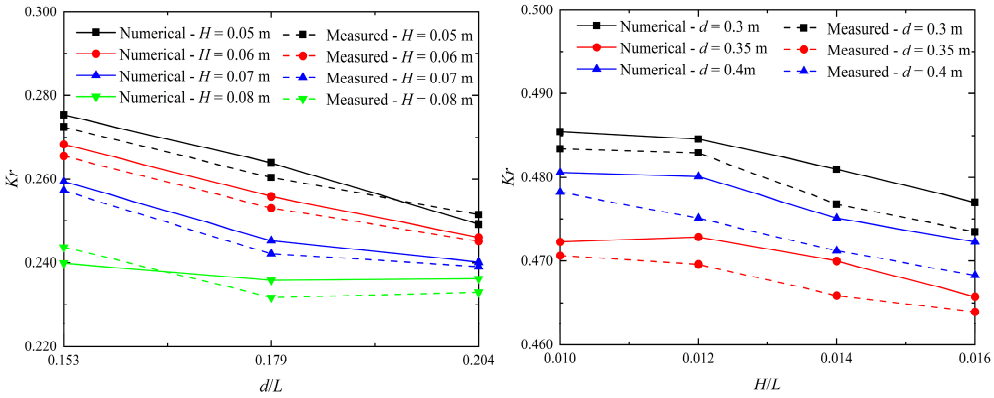

Figure 18. Variations of wave relative coefficient with various (**left panel**) relative water depth and (**right panel**) wave steepness.

Figure 18 illustrates how the wave reflection coefficient is affected by wave steepness, with an increase in steepness leading to a reduction in the reflection coefficient. The correlation between H/L and K_r exhibits a monotonic decline across various water depth scenarios. The simulated K_r and H/L align well with the experimental results.

Figure 19 delineates the impact of ξ on K_r across various water depth conditions. As ξ escalates, there is a corresponding increase in the wave reflection coefficient. This correlation is monotonically progressive and is observed across diverse water depth settings.

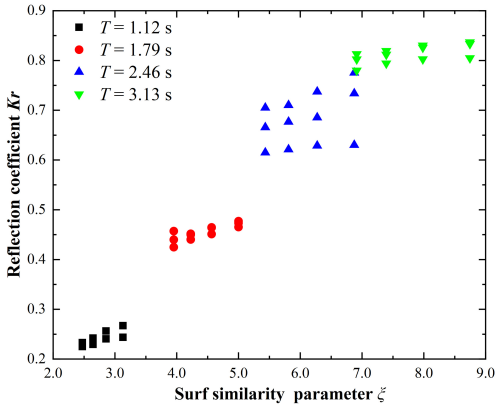

Figure 19. Scatterplot of wave reflection coefficient changing with surf similarity parameter.

5. Conclusions and Recommendations

This research developed a 3D wave computational model to explore wave run-up and reflection characteristics of a new ecological quadrangular hollow block. The model was verified by a physical flume test, which shows that the model has a good ability to simulate wave-block interaction actions. The outcomes of this investigation are encapsulated and synthesized in the subsequent points:

(1) In the "bare" flume, the computational model's series of water level fluctuations is juxtaposed with experimental data. The root mean square errors of R/H and K_r are 0.2909 m and 0.0770. The verification results demonstrate that the new ecological quadrilateral hollow block's wave run-up and reflection are reliably predicted by the established numerical model.

(2) The mean discrepancy in wave run-up and reflection coefficients across the three mesh configurations (e.g., 0.005 m, 0.0025 m, and 0.00125 m) is 8.91%. The investigation delves into the variations in water surface elevation, velocity field, and dynamic pressure field when the wave interacts with the new ecological quadrilateral hollow block at the three mesh sizes. The findings indicate that the water surface elevation data from the coarse mesh shows a greater deviation from the observed values compared to the finer meshes, whereas the mesh size exerts a minimal influence on the velocity and dynamic pressure fields.

(3) R/H escalates with increases in wave height, period, and relative water depth, as well as wave steepness. Conversely, the reflection coefficient diminishes as H, d/L, and H/L augment.

This research endeavored to analyze the dynamic interplay between wave run-up and reflection coefficients with a new ecological quadrangular block amidst regular wave conditions. Indeed, the regular wave simplifies the study situation. The actual wave conditions are mostly irregular, and the wave conditions are more complex. In the future study, it will be considered for the hydrodynamic characteristics of the new ecological quadrangular hollow blocks under irregular wave action.

Author Contributions: Conceptualization, Y.W., D.L., J.Y. and M.M.; Methodology, Y.W. and J.Y.; Software, Y.W.; Validation, D.L.; Investigation, Y.W.; Formal Analysis, Y.W.; Resources, D.L. and H.Z. (Haitao Zhao); Data Curation, Y.W.; Writing—Original Draft, Y.W.; Writing—Review & Editing, M.M., J.H. and H.Z. (Hongwu Zhang); Visualization, D.L. and J.Y.; Supervision, D.L., F.B., J.Y. and M.M.; Project Administration, D.L., F.B., J.H. and H.Z. (Haitao Zhao); Funding Acquisition, D.L., H.Z. (Haitao Zhao) and F.B. All authors have read and agreed to the published version of the manuscript.

Funding: This research was funded by the Zhejiang University of Water Resources and Electric Power (XKY2023012), the Key Laboratory for Technology in Rural Water Management of Zhejiang Province (ZJWEU-RWM-202101), the Zhejiang Provincial Natural Science Foundation of China (LZJWZ22C030001; LZJWZ22E090004; ZJWZ23E090009), the Zhejiang Provincial Department of Water Resources Water Resources Water Science and Technology Project (RB2115), the National Key Research and Development Program of China (2016YFC0402502), and the Open Fund of Key Laboratory of Marine Spatial Resource Management Technology, Ministry of Natural Resources, Zhejiang Province, China (KF-2022-110), Dr. M. Mao was supported by the Key R&D Program of Shandong Province, China (2022CXPT019).

Data Availability Statement: The data presented in this study are available upon request from the corresponding author.

Acknowledgments: The authors acknowledge the editors and anonymous reviewers for their valuable comments and suggestions.

Conflicts of Interest: The authors declare no conflict of interest.

References

1. Bakker, P.; van den Berge, A.; Hakenberg, R.; Klabbers, M.; Muttray, M.; Reedijk, B.; Rovers, I. Develpoment of concrete breakwater armour units. In Proceedings of the 1st Coastal, Estuary and Offshore Engineering Specialty Conference of the Canadian Society for Civil Engineering, Moncton, NB, Canada, 4–7 June 2003.
2. Giridhar, G.; Reddy, M.G.M. Hydrodynamic study of energy dissipation blocks on reduction of wave run-up and wave reflection. *Aquat. Procedia* **2015**, *4*, 281–286. [CrossRef]
3. Zanuttigh, B.; van der Meer, J.W. Wave reflection from coastal structures in design conditions. *Coast. Eng.* **2008**, *55*, 771–779. [CrossRef]
4. Seelig, W.N.; Ahrens, J.P. *Estimation of Wave Reflection and Energy Dissipation Coefficients for Beaches, Armours, and Breakwaters*; Army Engineer Research and Development Center (ERDC): Vicksburg, MI, USA, 1981.
5. Safari, I.; Mouazé, D.; Ropert, F.; Haquin, S.; Ezersky, A. Experimental Study to Determine Forces Acting on Starbloc Armor Units and Velocities Occurring in a Single-Layer Rubble Mound Breakwater under Regular Waves. *J. Waterw. Port Coast. Ocean Eng.* **2022**, *148*, 04022007. [CrossRef]
6. Yuksel, Y.; van Gent, M.R.; Cevik, E.; Kaya, A.H.; Guner, H.A.A.; Yuksel, Z.T.; Gumuscu, I. Stability of high density cube armoured breakwaters. *Ocean Eng.* **2022**, *253*, 111317. [CrossRef]
7. Pardo, V.; Herrera, M.P.; Molines, J.; Medina, J.R. Placement test, porosity, and randomness of cube and cubipod armor layers. *J. Waterw. Port Coast. Ocean Eng.* **2014**, *140*, 04014017. [CrossRef]
8. Park, Y.H.; Oh, Y.M.; Ahn, S.M.; Han, T.H.; Kim, Y.T.; Suh, K.D.; Won, D. Development of a new concrete armor unit for high waves. *J. Coast. Res.* **2019**, *35*, 719–728. [CrossRef]
9. Wehlitz, C.; Schoonees, J.S. Hydraulic stability of the new Cubilok™ armour unit on a 3:4 slope. *Coast. Eng.* **2023**, *183*, 0378–3839. [CrossRef]
10. Demirel, V.; Wang, S. An efficient boundary element method for two-dimensional transient wave propagation problems. *Appl. Math. Model.* **1987**, *11*, 411–416. [CrossRef]
11. Belibassakis, K.A. A boundary element method for the hydrodynamic analysis of floating bodies in variable bathymetry regions. *Eng. Anal. Bound. Elem.* **2008**, *32*, 796–810. [CrossRef]
12. Troch, P.; Li, T.Q.; De Rouck, J.; Ingram, D. Wave interaction with a sea dike using a vof finite-volume method. In Proceedings of the 13th International Offshore and Polar Engineering Conference, Honolulu, HI, USA, 25–30 May 2003; pp. 325–332.
13. Jose, J.; Choi, S.J.; Giljarhus, K.E.; Gudmestad, O.T. A comparison of numerical simulations of breaking wave forces on a monopile structure using two different numerical models based on finite difference and finite volume methods. *Ocean Eng.* **2017**, *137*, 78–88. [CrossRef]
14. Xiang, T.; Istrati, D. Assessment of extreme wave impact on coastal decks with different geometries via the arbitrary lagrangia-neulerian method. *Mar. Sci. Eng.* **2021**, *9*, 1342. [CrossRef]
15. Xiang, T.; Istrati, D.; Yim, S.C.; Buckle, I.G.; Lomonaco, P. Tsunami loads on a representative coastal bridge deck: Experimental study and validation of design equations. *Waterw. Port Coast. Ocean Eng.* **2020**, *146*, 04020022. [CrossRef]
16. Istrati, D.; Hasanpour, A.; Buckle, I. Numerical investigation of tsunami-borne debris damming loads on a coastal bridge. In Proceedings of the 17th World Conference on Earthquake Engineering, Sendai, Japan, 13–18 September 2020.
17. Istrati, D.; Buckle, I.G. *Tsunami Loads on Straight and Skewed Bridges—Part 2: Numerical Investigation and Design Recommendations*; Oregon Department of Transportation Research Section: Salem, OR, USA, 2021.

18. Arikawa, T.; Ishikawa, N.; Beppu, M.; Tatesawa, H. Collapse mechanisms of seawall due to the March 2011 Japan tsunami using the MPS method. *Int. J. Prot. Struct.* **2012**, *3*, 457–476. [CrossRef]
19. Monaghan, J.J. Simulating free surface flows with SPH. *J. Comput. Phys.* **1994**, *110*, 399–406. [CrossRef]
20. Zijlema, M.; Stelling, G.; Smit, P. SWASH: An operational public domain code for simulating wave fields and rapidly varied flows in coastal waters. *Coast. Eng.* **2011**, *58*, 992–1012. [CrossRef]
21. Gomez-Gesteira, M.; Rogers, B.D.; Crespo, A.J.; Dalrymple, R.A.; Narayanaswamy, M.; Dominguez, J.M. SPHysics–development of a free-surface fluid solver—Part 1: Theory and formulations. *Comput. Geosci.* **2012**, *48*, 289–299. [CrossRef]
22. Gómez-Gesteira, M.; Cerqueiro, D.; Crespo, C.; Dalrymple, R. Green water overtopping analyzed with a SPH model. *Ocean Eng.* **2005**, *32*, 223–238. [CrossRef]
23. Dalrymple, R.A.; Rogers, B.D. Numerical modeling of water waves with the SPH method. *Coast. Eng.* **2006**, *53*, 141–147. [CrossRef]
24. Crespo, A.J.; Gómez-Gesteira, M.; Dalrymple, R.A. Modeling dam break behavior over a wet bed by a SPH technique. *J. Waterw. Port Coast. Ocean Eng.* **2008**, *134*, 313–320. [CrossRef]
25. Barreiro, A.; Crespo, A.; Domínguez, J.; Gómez-Gesteira, M. Smoothed particle hydrodynamics for coastal engineering problems. *Comput. Struct.* **2013**, *120*, 96–106. [CrossRef]
26. Dentale, F.; Reale, F.; Di Leo, A.; Carratelli, E.P. A CFD approach to rubble mound breakwater design. *Int. J. Nav. Archit. Ocean Eng.* **2018**, *10*, 644–650. [CrossRef]
27. Peng, C.; Wang, H.; Zhang, H.; Chen, H. Parametric design and numerical investigation of hydrodynamic characteristics of a new type of armour block TB-CUBE based on SPH method. *J. Mar. Sci. Eng.* **2022**, *10*, 1116. [CrossRef]
28. Ding, D.; Ouahsine, A.; Xiao, W.; Du, P. CFD/DEM coupled approach for the stability of caisson-type breakwater subjected to violent wave impact. *Ocean Eng.* **2021**, *223*, 108651. [CrossRef]
29. Scaravaglione, G.; Latham, J.P.; Xiang, J.S. Numerical Model Study of Prototype Drop Tests on Cube and Cubipod® Concrete Armor Units Using the Combined Finite–Discrete Element Method. *J. Mar. Sci. Eng.* **2021**, *9*, 460. [CrossRef]
30. Mitsui, J.; Altomare, C.; Crespo, A.J.; Domínguez, J.M.; Martínez-Estévez, I.; Suzuki, T.; Kubota, S.-I.; Gómez-Gesteira, M. DualSPHysics modelling to analyse the response of Tetrapods against solitary wave. *Coast. Eng.* **2023**, *183*, 104315. [CrossRef]
31. Zhao, H.; Ding, F.; Ye, J.; Jiang, H.; Chen, W.; Gu, W.; Yu, G.; Li, Q. Physical Experimental Study on the Wave Reflection and Run-Up of a New Ecological Hollow Cube. *J. Mar. Sci. Eng.* **2024**, *12*, 664. [CrossRef]
32. Goda, Y.; Suzuki, Y. Estimation of incident and reflected waves in random wave experiments. In Proceedings of the 15th Coastal Engineering Conference, Honlulu, HI, USA, 11–17 July 1976; Volume 1, pp. 828–845.
33. Ma, Y.; Zhu, L.; Peng, Z.; Xue, L.; Zhao, W.; Li, T.; Lin, S.; Bouma, T.J.; Hofland, B.; Dong, C.; et al. Wave attenuation by flattened vegetation (*Scirpus mariqueter*). *Front. Mar. Sci.* **2023**, *10*, 1106070. [CrossRef]
34. Bouma, T.J.; Vries, M.D.; Low, E.; Kusters, L.; Herman, P.M.; Tanczos, I.C.; Temmerman, S.; Hesselink, A.; Meire, P.; Regenmortel, S.V. Flow hydrodynamics on a mudflat and in salt marsh vegetation: Identifying general relationships for habitat characterisations. *Hydrobiologia* **2005**, *540*, 259–274. [CrossRef]
35. Anderson, M.E.; Smith, J.M. Wave attenuation by flexible, idealized salt marsh vegetation. *Coast. Eng.* **2014**, *83*, 82–92. [CrossRef]
36. Maza, M.; Lara, J.L.; Losada, I.J. A paradigm shift in the quantification of wave energy attenuation due to saltmarshes based on their standing biomass. *Sci. Rep.* **2022**, *12*, 13883. [CrossRef]
37. Weller, H.G.; Tabor, G.; Jasak, H.; Fureby, C. A tensorial approach to computational continuum mechanics using object-oriented techniques. *Comput. Phys.* **1998**, *12*, 620–631. [CrossRef]
38. Ferziger, J.H.; Perić, M. *Computational Methods for Fluid Dynamics*; Springer: New York, NY, USA, 2002.
39. Issa, R.I. Solution of the implicitly discretised fluid flow equations by operator-splitting. *J. Comput. Phys.* **1986**, *62*, 40–65. [CrossRef]
40. Lara, J.L.; Garcia, N.; Losada, I.J. RANS modelling applied to random wave interaction with submerged permeable structures. *Coast. Eng.* **2006**, *53*, 395–417. [CrossRef]
41. Jacobsen, N.G.; Fuhrman, D.R.; Fredsøe, J. A wave generation toolbox for the open-source CFD library: OpenFoam®. *Int. J. Numer. Methods Fluids* **2012**, *70*, 1073–1088. [CrossRef]
42. Vanneste, D.; Troch, P. 2D numerical simulation of large-scale physical model tests of wave interaction with a rubble-mound breakwater. *Coast. Eng.* **2015**, *103*, 22–41. [CrossRef]
43. Ye, J.; Shan, J.; Zhou, H.; Yan, N. Numerical modelling of the wave interaction with armour breakwater built on reclaimed coral reef islands in the South China Sea—Experimental verification. *Ocean Eng.* **2021**, *235*, 109325. [CrossRef]
44. Schoonees, T.; Kerpen, N.B.; Schlurmann, T. Full-scale experimental study on wave reflection and run-up at stepped revetments. *Coast. Eng.* **2022**, *172*, 104045. [CrossRef]

45. EurOtop. *Manual on Wave Overtopping of Sea Defences and Related Structures: An Overtopping Manual Largely Based on European Research, but for Worldwide Application*, 2nd ed.; Van der Meer, J.W., Allsop, N., Bruce, T., De Rouck, J., Kortenhaus, A., Pullen, T., Schüttrumpf, H., Troch, P., Zanuttigh, B., Eds.; EurOtop: Warszawa, Poland, 2018. Available online: https://www.overtopping-manual.com (accessed on 10 November 2024).
46. Di Risio, M.; Bruschi, A.; Lisi, I.; Pesarino, V.; Pasquali, D. Comparative analysis of coastal flooding vulnerability and hazard assessment at national scale. *J. Mar. Sci. Eng.* **2017**, *5*, 51. [CrossRef]
47. Mahdavi-Meymand, A.; Zounemat-Kermani, M.; Sulisz, W.; Silva, R. Modeling of wave run-up by applying integrated models of group method of data handling. *Sci. Rep.* **2022**, *12*, 8279. [CrossRef]
48. Elbisy, M.S. Estimation of regular wave run-up on slopes of perforated coastal structures constructed on sloping beaches. *Ocean Eng.* **2015**, *109*, 60–71. [CrossRef]
49. Van der Meer, J.W.; Stam, C.J.M. Wave runup on smooth and rock slopes of coastal structures. *Waterw. Port Coast. Ocean Eng.* **1992**, *118*, 534–550. [CrossRef]
50. Muttray, M.; Oumeraci, H.; Oever, E. Wave reflection and wave run-up at rubble mound breakwaters. In Proceedings of the 30th International Conference on Coastal Engineering, ICCE 2006, San Diego, CA, USA, 3–8 September 2006; Volume 5, pp. 4314–4324.
51. Schimmels, S.; Vousdoukas, M.; Wziatek, D.; Becker, K.; Gier, F.; Oumeraci, H. Wave run-up observations on revetments with different porosities. *Coast. Eng.* **2012**, *33*, 1–14. [CrossRef]
52. Hunt, I.A., Jr. Design of seawalls and breakwaters. *J. Waterw. Harb. Div.* **1959**, *85*, 123–152. [CrossRef]
53. Saville, T., Jr. Wave run-up on shore structures. *J. Waterw. Harb. Div.* **1956**, *82*, 925-1–925-14. [CrossRef]
54. Whalin, R. Run-up and stability of intermediate period water waves at Monterey California. *J. Dyn. Waves Civ. Eng.* **1971**, 265–291.